Smart Readout of Nondestructive Image Sensors with Single Photon-Electron Sensitivity

Fernando Chierchie[1], Guillermo Fernandez Moroni[2,*], Leandro Stefanazzi,[2] Eduardo Paolini[1], Javier Tiffenberg,[2] Juan Estrada,[2] Gustavo Cancelo,[2] and Sho Uemura[3]

[1]*Instituto de Investigaciones en Ingeniería Eléctrica "Alfredo Desages" (IIIE),*
Departamento de Ingeniería Eléctrica y de Computadoras. CONICET and Universidad Nacional del Sur (UNS),
Bahía Blanca 8000, Argentina
[2]*Fermi National Accelerator Laboratory, Batavia, Illinois 60510-5011, USA*
[3]*School of Physics and Astronomy, Tel-Aviv University, Tel-Aviv 69978, Israel*

Image sensors with nondestructive charge readout provide single-photon or single-electron sensitivity, but at the cost of long readout times. We present a smart readout technique to allow the use of these sensors in visible light and other applications that require faster readout times. The method optimizes the readout noise and time by changing the number of times pixels are read out either statically, by defining an arbitrary number of regions of interest in the array, or dynamically, depending on the charge or energy of interest in the pixel. This technique is tested in a Skipper CCD showing that it is possible to obtain deep subelectron noise, and therefore, high resolution of quantized charge, while dynamically changing the readout noise of the sensor. These faster, low noise readout techniques show that the skipper CCD is a competitive technology even where other technologies such as electron multiplier charge coupled devices, silicon photo multipliers, etc. are currently used. This technique could allow skipper CCDs to benefit new astronomical instruments, quantum imaging, exoplanet search and study, and quantum metrology.

Introduction.—Single-photon and single-electron resolution semiconductor sensors have proven to be a major scientific breakthrough overcoming the limitation imposed by readout noise [1–3]. Some technologies, such as electron multiplying charge coupled device (EMCCD) [4] or silicon photomultipliers [5], are based on charge multiplication. More recent ones use nondestructive readout techniques to average several observations of the collected charge [6–8]. Arbitrary precision is obtained at the expense of increasing the number of samples (N from here) and thus the readout time. Assuming independent measurements, the noise is reduced following [9] $\sigma_0/\sqrt{N}$, where σ_0 is the root mean squared error for one measurement of the charge. In particular, the Skipper CCD [6,9] uses a floating sense node to isolate the charge packet from the first amplification stage which allows us to make multiple measurements, using the correlated double sampling (CDS) method [10], to get single-electron resolution pixel readout. In recent years, many applications such as dark matter searches [11], neutrino detection [12], and study of properties of semiconductor materials [13] have exploited this capability, but others such as quantum imaging [14], astronomical terrestrial instruments [15], satellite missions for exoplanet searches [16], and sub-shot-noise microscopy [17], remain inaccessible for the Skipper CCD due to the long readout time.

The readout noise is not always the limiting factor. Other processes produce statistical fluctuations that are added in quadrature with the electronic noise and contribute to the total uncertainty. Among these processes we can mention intrinsic factors of the sensor like quantum efficiency, leakage current, charge transfer and collection inefficiencies, crystal ionization mechanism, etc; and extrinsic factors, like the Poisson statistics of photon arrival, natural background ionizing particles, etc. [10,18]. When these dominate, there is no benefit to reducing the readout noise by increasing the readout time. In this Letter a smart readout technique to reduce readout time by changing the readout noise based on available information for the specific application is presented. Experimental results using an Skipper CCD are reported, but the technique may be also applied to any existing or future sensors with nondestructive readout (either with active or passive pixels) to adapt either the readout time or the dynamic range of the measuring system.

Description of the technique.—Figure 1(a) shows a conceptual diagram. The block "baseline and smart readout" confers intelligence to the output stage of the CCD to perform an adaptive modification of the number of measurements N of the charge q in each pixel using information of the sensor's parameters, the physics source of interest (reference inputs) and information of the current pixel. The easier strategy is to optimize N according to the position of the pixel in the array (x, y). If the incoming photon flux illuminates a specific region, N can be increased for that region, while faster readout (and higher noise) can be used for the remaining area. This strategy adjusts the readout
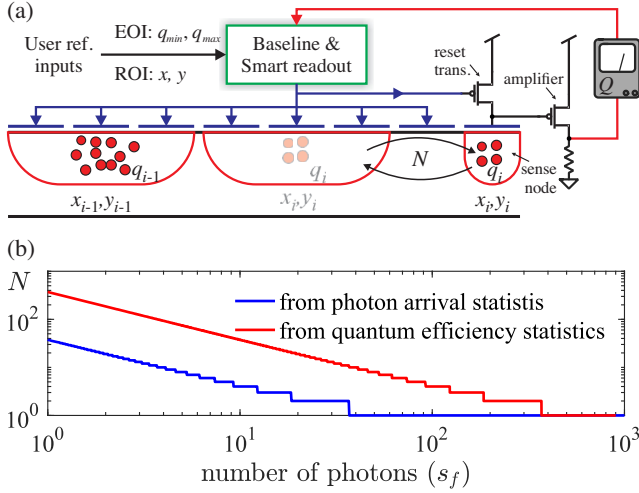
FIG. 1. (a) Conceptual design; (b) number of samples per pixel N for the same fractional contribution from readout noise to photon uncertainty as a function of s_f; assuming $k = 0.95$, $QE = 0.9$, and $\sigma_0 = 2$ electrons, or, equivalently, photons.

time and noise (or equivalently, adjusts the dynamic range) based on regions of interest (ROI) which are previously known for the application. Another approach is to update N depending on the range of charge (q_{min}, q_{max}) or deposited energy being measured, i.e., based on the energy of interest (EOI).

For example, typical applications currently limited for the Skipper CCD involve visible or infrared light detection. These systems are intrinsically limited by photon statistics, which can be described by a binomial distribution (attributed to the collection efficiency of the detector) together with a Poisson distribution (attributed to photon arrival statistics).

Two scenarios are considered to show the EOI strategy: (i) a system limited by Poisson uncertainty of photon arrival, as any astronomical instrument [19], assuming ideal collection of photons in the sensor; (ii) a system limited by photon detection uncertainty, due to quantum efficiency ($QE < 1$), following a binomial distribution and assuming no Poisson arrival uncertainty, as expected in applications using entangled photons [20]. In both systems, the signal to noise ratio (SNR) is $s_f / \sqrt{\sigma_f^2 + \sigma_0^2 / N}$, where s_f is the expected number of collected photons and σ_f is the standard deviation in the expected number of collected photons [$\sigma_f = \sqrt{s_f}$ and $\sigma_f = \sqrt{s_f(1 - QE)}$ for each example, respectively]. The number of samples per pixel N can be tuned to get a desired SNR for each number of collected photons (or equivalently collected charge). If N is adjusted to produce a SNR for each pixel equal to k times ($k < 1$) its SNR without readout noise ($\sigma_0 = 0$), so that the fractional contribution of readout noise to photon uncertainty is the same for every pixel, then,

$$N = \frac{\sigma_0^2 k^2}{\sigma_f^2 (1 - k^2)}, \quad \begin{cases} \sigma_f^2 = s_f & \text{Poisson} \\ \sigma_f^2 = s_f(1 - QE) & \text{Binomial.} \end{cases} \quad (1)$$

As shown in Fig. 1(b), increasing N significantly decreases the uncertainty on the number of collected photons for pixels collecting fewer than 40 photons for Poisson statistics and 400 for binomial statistics. For pixels with more than this number of photons, Eq. (1) finds that $N = 1$ is sufficient to meet the goal defined by k.

This shows that an smart strategy has a big potential in reducing the readout time and tuning the dynamic range of the system for pixels with relatively small charge packets (0.1% and 0.4% of the full pixel capacity, as tested for similar devices [21]) which demands larger N values to meet the SNR requirement. For a general application, assuming a uniform distribution of pixel charge values between $1e^-$ and $100 \times 10^3 e^-$, the result in Fig. 1(b) gives that the readout time with a smart strategy is 2.6% and 0.26% that of the nonsmart strategy (all pixels read out with the highest N value), in the Poisson and binomial scenarios, respectively.

Implementation challenges.—Although changing the number of samples N read per pixel seems straightforward, this requires changing the clock signals (twenty in our case) of the CCD "on the fly." Because the CCD is a highly coupled device and the voltage swings of the clocks are on the order of tens of volts, changes to the clocks cause variations in the baseline of the video signal that, if not treated properly, introduce a systematic error in the determination of the pixel charge. Since the sensitivity of the CCD is in the order of 2μ V/e^-, this imposes a sub-ppm control of the errors. We develop a calibration technique that can be performed on- and off-line so that N can be changed without increasing the systematic error due to baseline variation.

Figure 2 shows a measurement of the baseline changes in the raw video signal, before pixel computation, due to the changing clocks signals applied to a skipper CCD. The exponential decay at $t = 0$ is caused by the vertical clocks applied before $t = 0$. The plateau that follows is caused by many consecutive pixels read out with $N = 1$. The slope within a single pixel, seen in the inset, will cause a nonzero pixel value, an effect that is present in every CCD. The exponential at $t \approx 0.2$ is caused by a change in the readout mode, from $N = 1$ to $N = 100$. The downward glitches seen for $t > 0.2$ correspond to the first measurement of each pixel, which has a different clocking compared to the next 99 measurements. Figure 2 shows a change of 0.1 V in the output signal base level (baseline), which exceeds by 5×10^4 times the expected signal for one electron ($\approx 2 \mu$V).

Baseline is present in any CCD; it is usually estimated by taking an overscan region (empty pixels obtained by reading more charge packets from the serial register than there are active pixels), and subtracted from each image [22]. A similar approach can be used for the ROI strategy
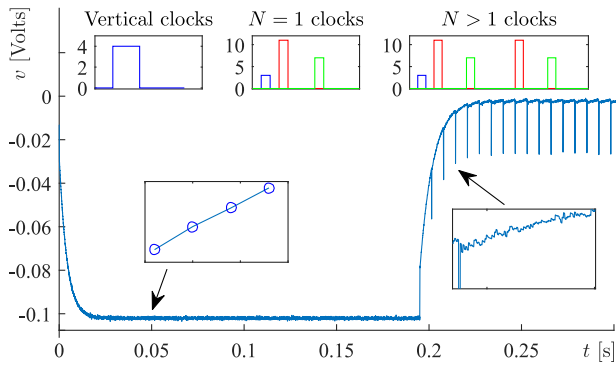
FIG. 2. Baseline of raw video signal in volts. Part of one row, the first 3039 pixels use $N = 1$ and the others $N = 100$. At the top, insets illustrate clock sequences and their voltage swings. At the bottom, enlarged regions of the baseline corresponding to the samples of a single pixel read with $N = 1$ at $t \approx 0.05$ and with $N = 100$ at $t \approx 0.215$.
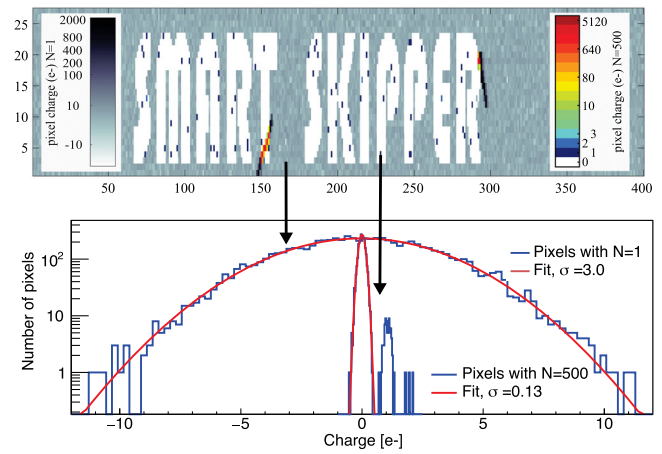

FIG. 3. Measurement using ROI technique. Pixels in the words have $N = 500$ (right scale); pixels outside the words have $N = 1$ (left scale). s_f was zero in most pixels, with some pixels having $s_f = 1, 2, 3$ or very large values for the two muon tracks that are observed.

[23], though this requires extra calibration time to acquire empty images for each ROI. On the other hand, the EOI strategy changes N on-line and requires corrected pixel values to be available during readout. Therefore it is mandatory to have a baseline compensation technique that can be applied on-line.

We developed a baseline correction technique based on the superposition of the effects of a group of control signals on the output video signal. An identification procedure is performed only once, and the baseline correction can be computed (on-line and off-line) as the superposition of the calibrated effects for any readout sequence, either under ROI or EOI. The identification procedure is performed in the pixel values and not in the raw video signal, thus simplifying the implementation as discussed in the Supplemental Material [24].

Experimental results.—The experimental proof of concept of the technique is done switching between $N = 1$ and $N = 500$ for ROI and EOI experiments. $N = 500$ results in deep subelectron noise operation and therefore any artifact introduced by the proposed adaptive readout would impact the measured total noise. Also, the jump between $N = 1$ or $N = 500$ produces a large change in the baseline allowing to test the capability of the readout routine to compensate for these perturbations.

Inside a dewar, the skipper-CCD is operated at high vacuum (approximately 10^{-4} mbar) and at a temperature of 140 K. The sensor is a fully depleted CCD developed by Lawrence Berkeley National Laboratory, LBNL [6]. The low threshold acquisition controller (LTA) [25] is used for readout and control.

We report three experiences: (i) ROI specified before the readout, (ii) EOI experiment choosing different charge ranges, and (iii) a combination of both: once a pixel is detected in EOI, a ROI to the right of that pixel is readout with large N to achieve subelectron noise.

For the on-line implementation of the EOI, the first measurement of the pixel is corrected by the baseline algorithm. If the value is within the charge range set by the user, $N - 1$ further samples are taken of the same pixel. However, if the first value is outside the range, the readout sequence continues with the next pixel. The complete baseline compensation is applied to the final image. For the ROI strategy the compensation is only applied to the final image. Further details can be found in the Supplemental Material [24].

Experiment with ROI: Figure 3 shows an image acquired with the proposed ROI technique. To show the versatility, ROIs were defined by the words "SMART SKIPPER": noise is $0.13e^-$ inside the letters and $3e^-$ outside. Both noise measurements are obtained by Gaussian fits of the histograms, as shown in the figure. This is the theoretical expected reduction of noise when going from $N = 1$ to $N = 500$: $\sigma_{P_{i,skp}} = \sigma_0/\sqrt{N} = 3/\sqrt{500} \approx 0.13$ which proves that the baseline compensation technique does not harm the sensor charge resolution.

Experiment with EOI: Figure 4 show an image taken with the proposed technique after a long exposure time to collect charge from intrinsic ionization in the sensor, with $N = 500$ for pixels with $0e^-$ to $42e^-$ and $N = 1$ for pixels with $< 0e^-$ or $> 42e^-$. Two notable regions are observed: part of the active region of the sensor with interacting particles and an overscan region starting in column 321. The resulting pattern of Skipper samples N is depicted at the bottom. Because of the long exposure, most of the active region is modestly charged and therefore read with $N = 500$. The exceptions are the energetic muon and electron tracks, where most pixels have charge greater than $42e^-$ and are automatically read with $N = 1$. In the overscan region mostly empty pixels are present resulting
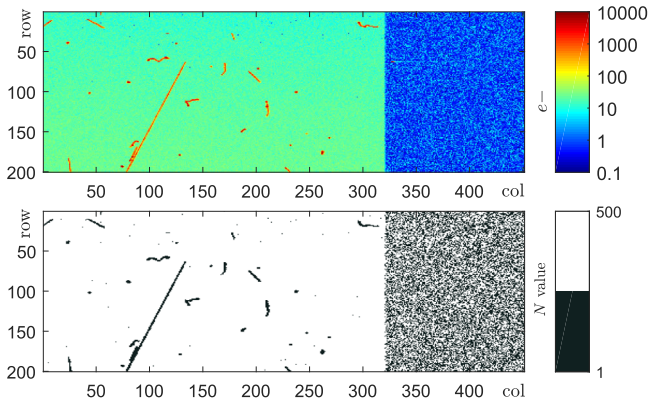
FIG. 4. (Top) Image using EOI technique. (Bottom) N for each pixel.

in a random pattern of $N = 1$ and $N = 500$ and showing the versatility of the system to change the value of N in every pixel.

Figure 5 shows two histograms in logarithmic scale as a result of applying the EOI technique in two different experiments. Peaks at integer numbers of electrons are clearly observed in two different charge intervals where charge quantization is achieved using $N = 500$.

In both measurements, the envelope of the histograms has two distinctive bumps: one around $0e^-$ from mostly empty pixels (mainly from the overscan) and another one centered at approximately $20e^-$ (from the active region). The latter shows, in logarithmic scale, the characteristic Poisson distribution.

A half Gaussian distribution is observed at the left of $0e^-$ in the histogram at the top. The green line shows a fit with a standard deviation $\sigma_0 = 3e^-$, which is the expected readout noise for $N = 1$. For $N = 500$ the results are depicted in red with a fit of the $20e^-$ peak. The standard deviation of the fit is $\sigma_{P_{i,skp}} = 0.13e^-$, again verifying the theoretical
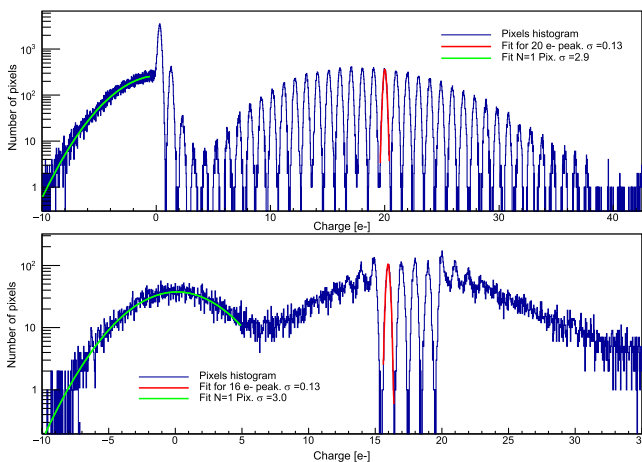
prediction for independent averaged measurements despite changing N dynamically based on the pixel charge. The histogram at the bottom, for charge in the interval $15e^-$ to $19e^-$, also shows the Gaussian fitting and the same noise performance.

Experiment combining ROI and EOI: We combine both ROI and EOI techniques using the ionization produced by a muon track to trigger subelectron pixel measurement.

The charge range is set between $52e^-$ and $6250e^-$ to avoid false trigger from dark current generation. If the charge of a pixel is in the range, the current and the following 99 pixels are read $N = 500$ times, independent of their charge value.

Figure 6 shows a fraction of the image where a muon was detected (straight line). The muon is seen mostly in red colors indicating hundreds or thousands of electrons deposited in those pixels. To the right of the muon, 99 pixels were also read with $N = 500$ samples per pixel; those pixels are observed as a white parallelogram ROI composed mostly of empty pixels (white pixels) and some pixels with $1,2,3,\cdots e^-$.

This experiment shows that it is possible to combine both techniques, which could be useful to study the charge generation around certain events of interest.

Scientific applications.—New astronomical instruments: The potential of the subelectron noise of the Skipper CCD is being explored for terrestrial astronomy [6,15] for signals with small SNR. Acquisitions with limited exposure time naturally produce low SNR observations where the impact of readout noise is high. Authors claim that a reduction of 100 in the readout time is still required, which is similar to the time reduction obtained by EOI in previous section in systems limited by photon arrival statistics. Moreover, for spectrography instruments where spectra are well defined areas in the sensor [26], a ROI strategy could further improve the readout speed. To quantitatively address this scenario we obtained a real image from the LDSS-3 [T. Diehl 2018, private communication], a high efficiency optical wide-field imager

FIG. 5. Pixel histograms for EOI technique. $N = 500$ for charge ranges $0e^-$ to $42e^-$ (top) and $15e^-$ to $19e^-$ (bottom).
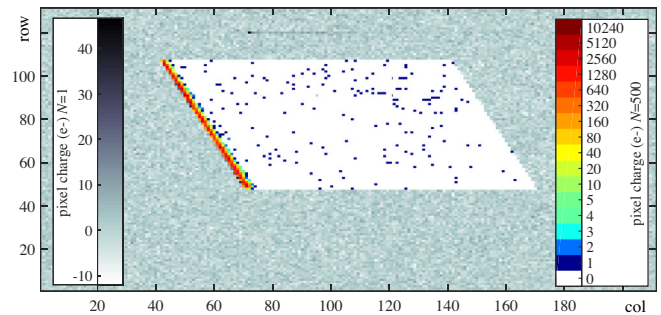

FIG. 6. Experiment combining ROI and EOI. Two color scales: on the left pixels with $N = 1$ and a noise of $3e^-$, and on the right pixels with $N = 500$ and a readout noise of $0.13e^-$ (and therefore quantized charge).

and multi-slit spectrograph [27]. The value N for each pixel based on the Poisson uncertainty was computed and resulted in a reduction of the readout time of a factor of 100.

Quantum imaging techniques: A pair of photons can exhibit spatial, spectral and polarization quantum entanglement. Spatial entanglement has been extensively explored for quantum communication [28]. Spontaneous parametric down-conversion crystals have eased the production of entangled pairs over a large number of positions [29] for example for ghost imaging [30,31]. Intensity correlation can be used for several other imaging techniques [32] such as fluorescence correlation spectroscopy [33]. Two-dimensional semiconductor devices provide a good sensor solution for these applications [34]. In particular, the single photon counting capability and large quantum efficiency of the Skipper CCD make it a promising technology in the field [14]. Moreover, as detailed in Ref. [32] on-chip noise sources impact the final measurable correlation of entangled photons, and therefore the EOI and ROI strategies can be used due to the high spatial and intensity correlation between entangled photons in two known regions of the image.

Exoplanet search and study: Direct imaging space telescopes for exoplanet detection and characterization are being planned [35]. One of the main goals for future missions is to search for near-infrared photons at 950 nm from water vapor in the atmosphere of potentially habitable planets. A sensor with large quantum efficiency and subelectron readout noise is required. The Skipper CCD has been identified by NASA as a promising technology that meets both requirements [16,35,36]. Moreover, the radiation hardness compared to EMCCD makes it more suitable for space missions. The main identified challenge is the slow readout time (≈ 20 min for 1 Mpixel array read by one amplifier at deep subelectron noise). According to Ref. [37] less than 200 hundred pixels per spectral element will be needed for the mission's spectrograph. To overcome the readout time limitation one possibility is to use the ROI strategy to directly focus on the key wavelengths and meet the 20 sec readout time constraint [36].

Electron pump for quantum metrology: Recently there has been a redefinition of the ampere by means of the charge of the electron [38,39]. One of the technological candidates for metrology is the single-electron transistor (SET) [40]. These quantum devices are operated at milli-Kelvin temperatures, which complicates the scaling required to achieve reasonable practical currents (in the order of 1 μA). The Skipper CCD is a promising technology for the development of a current source with single-electron manipulation. Although scaling is still a challenge, one advantage is its higher temperature of operation (in the order of 100 K). To reach an stable average current a smart readout technique is mandatory, since charge should be measured and drained out of the device at a rate that depends on the actual charge packet measurement [41].

---

[*]Corresponding author.
  gfmoroni@fnal.gov

[1] E. Simoen and C. Claeys, Solid-State Electron. **43**, 865 (1999).

[2] J. R. Janesick, T. S. Elliott, A. Dingiziam, R. A. Bredthauer, C. E. Chandler, J. A. Westphal, and J. E. Gunn, in Charge-Coupled Devices and Solid State Optical Sensors, edited by M. M. Blouke, International Society for Optics and Photonics Vol. 1242 (SPIE, Bellingham, WA, 1990), pp. 223–237.

[3] A. Boukhayma, *Ultra Low Noise CMOS Image Sensors*, Springer Theses (Springer International Publishing, New York, 2017).

[4] J. Hynecek and T. Nishiwaki, IEEE Trans. Electron Devices **50**, 239 (2003).

[5] P. Buzhan, B. Dolgoshein, L. Filatov, A. Ilyin, V. Kantzerov, V. Kaplin, A. Karakash, F. Kayumov, S. Klemin, E. Popova, and S. Smirnov, Nucl. Instrum. Methods Phys. Res., Sect. A **504**, 48 (2003).

[6] J. Tiffenberg, M. Sofo-Haro, A. Drlica-Wagner, R. Essig, Y. Guardincerri, S. Holland, T. Volansky, and T.-T. Yu, Phys. Rev. Lett. **119**, 131802 (2017).

[7] K. D. Stefanov, M. J. Prest, M. Downing, E. George, N. Bezawada, and A. D. Holland, Sensors **20**, 2031 (2020).

[8] M. W. Bautz, B. E. Burke, M. Cooper, D. Craig, R. F. Foster, C. E. Grant, B. J. LaMarr, C. Leitz, A. Malonis, E. D. Miller, G. Prigozhin, D. Schuette, V. Suntharalingam, and C. Thayer, J. Astron. Telesc. Instrum. Syst. **5**, 021015 (2019).

[9] G. Fernández Moroni, J. Estrada, G. Cancelo, S. E. Holland, E. E. Paolini, and H. Thomas Diehl, Exp. Astron. **34**, 43 (2012).

[10] J. R. Janesick, *Scientific Charge-Coupled Devices* (SPIE Press, Bellingham, WA, 2001), Vol. 83.

[11] L. Barak *et al.* (SENSEI Collaboration), Phys. Rev. Lett. **125**, 171802 (2020).

[12] J. C. D'Olivo, C. Bonifazi, D. Rodrigues, and G. F. Moroni, in XXIX International Conference in Neutrino Physics (2020), poster 521, https://nusoft.fnal.gov/nova/nu2020postersession/pdf/posterPDF-521.pdf.

[13] D. Rodrigues, K. Andersson, M. Cababie, A. Donadon, G. Cancelo, J. Estrada, G. Fernández Moroni, R. Piegaia, M. Senger, M. S. Haro *et al.*, Nucl. Instrum. Methods Phys. Res., Sect. A **1010**, 165511 (2021).

[14] J. Estrada, R. Harnik, D. Rodrigues, and M. Senger, PRX Quantum **2**, 030340 (2021).

[15] A. Drlica-Wagner, E. M. Villalpando, J. O'Neil, J. Estrada, S. Holland, N. Kurinsky, T. Li, G. F. Moroni, J. Tiffenberg, and S. Uemura, in X-Ray, Optical, and Infrared Detectors for Astronomy IX, edited by A. D. Holland and J. Beletic,

International Society for Optics and Photonics Vol. 11454 (SPIE, Bellingham, WA, 2020), pp. 210–223.

[16] B. J. Rauscher, S. E. Holland, L. R. Miko, and A. Waczynski, in UV/Optical/IR Space Telescopes and Instruments: Innovative Technologies and Concepts IX, edited by A. A. Barto, J. B. Breckinridge, and H. P. Stahl, International Society for Optics and Photonics Vol. 11115 (SPIE, Bellingham, WA, 2019), pp. 382–386.

[17] N. Samantaray, I. Ruo-Berchera, A. Meda, and M. Genovese, Light Sci. Appl. **6**, e17005 (2017).

[18] D. E. Groom, S. E. Holland, M. E. Levi, N. P. Palaio, S. Perlmutter, R. J. Stover, and M. Wei, in *Proc. SPIE 3649, Sensors, Cameras, and Systems for Scientific/Industrial Applications* (SPIE, Bellingham, WA, 1999), Vol. 3649, pp. 80–90, https://doi.org/10.1117/12.347079.

[19] J. R. Janesick, *Photon Transfer* (SPIE, Bellingham, WA, 2007), https://doi.org/10.1117/3.725073.

[20] G. Brida and I. Ruo Berchera, Nat. Photonics **4**, 227 (2010).

[21] H. T. Diehl *et al.*, in High Energy, Optical, and Infrared Detectors for Astronomy III, edited by D. A. Dorn and A. D. Holland, International Society for Optics and Photonics Vol. 7021 (SPIE, Bellingham, WA, 2008), pp. 86–96.

[22] C. B. Roundy, in *Proceedings of the 10th Meeting on Optical Engineering in Israel*, edited by I. Shladov and S. R. Rotman, International Society for Optics and Photonics Vol. 3110 (SPIE, Bellingham, WA, 1997), pp. 860–879.

[23] F. Chierchie, G. F. Moroni, L. Stefanazzi, C. Chavez, E. Paolini, G. Cancelo, M. S. Haro, J. Tiffenberg, J. Estrada, and S. Uemura, arXiv:2012.10414.

[24] See Supplemental Material at http://link.aps.org/supplemental/10.1103/PhysRevLett.127.241101 for smart readout of nondestructive image sensors with single-photon sensitivity.

[25] G. I. Cancelo, C. Chavez, F. Chierchie, J. Estrada, G. Fernandez-Moroni, E. E. Paolini, M. S. Haro, A. Soto, L. Stefanazzi, J. Tiffenberg, K. Treptow, N. Wilcer, and T. J. Zmuda, J. Astron. Telesc. Instrum. Syst. **7**, 015001 (2021).

[26] S. B. Howell, *Handbook of CCD Astronomy* (Cambridge University Press, Cambridge, England, 2006), Vol. 5.

[27] LDSS3, The low dispersion survey spectrograph (2021 (accessed October 19, 2021)), http://www.lco.cl/wp-content/uploads/2021/02/LDSS3handout2021.pdf.

[28] Z.-S. Yuan, X.-H. Bao, C.-Y. Lu, J. Zhang, C.-Z. Peng, and J.-W. Pan, Phys. Rep. **497**, 1 (2010).

[29] A. A. Malygin, A. N. Penin, and A. V. Sergienko, Sov. Phys. Dokl. **30**, 227 (1985).

[30] M. J. Padgett and R. W. Boyd, Phil. Trans. R. Soc. A **375**, 20160233 (2017).

[31] T. B. Pittman, Y. H. Shih, D. V. Strekalov, and A. V. Sergienko, Phys. Rev. A **52**, R3429 (1995).

[32] H. Defienne, M. Reichert, and J. W. Fleischer, Phys. Rev. Lett. **120**, 203604 (2018).

[33] F. Bestvater, Z. Seghiri, M. Kang, N. Gröner, J.-Y. Lee, K.-B. Im, and M. Wachsmuth, Opt. Express **18**, 23818 (2010).

[34] A. Orieux, M. A. M. Versteegh, K. D. Jns, and S. Ducci, Rep. Prog. Phys. **80**, 076001 (2017).

[35] B. Crill and N. Siegler, Jet Propulsion Laboratory Publications D-102506 (2018), https://exoplanets.nasa.gov/internal_resources/1123.

[36] B. J. Rauscher, S. E. Holland, L. R. Miko, and A. Waczynski, Radiation Tolerant, Photon Counting, Visible and Near-IR Detectors for SpaceCoronagraphs and Starshades (2019), https://exoplanets.nasa.gov/internal_resources/1390/.

[37] C. C. Stark *et al.*, J. Astron. Telesc. Instrum. Syst. **5**, 024009 (2019).

[38] B. I. des Poids et Mesure, Mise en pratique for the Definition of the Ampere and Other Electric Units in the SI (2019), appendix 2.

[39] H. Scherer and H. W. Schumacher, Ann. Phys. (Berlin) **531**, 1800371 (2019).

[40] S. Giblin, M. Kataoka, J. Fletcher, P. See, T. Janssen, J. Griffiths, G. Jones, I. Farrer, and D. Ritchie, Nat. Commun. **3**, 930 (2012).

[41] J. Tiffenberg and G. F. Moroni, Pinning down the ampere with a supersensitive particle detector (2020 (accessed April 29, 2021)), https://news.fnal.gov/2020/10/pinning-down-the-ampere-with-a-supersensitive-particle-detector/.

SUPPLEMENTAL MATERIALS for: Smart readout of nondestructive image sensors with single-photon sensitivity

READOUT ELECTRONICS

The low threshold acquisition controller (LTA) [1] was used for the developing and testing of the proposed technique. Figure 1 depicts a block diagram of the electronics. The data processing and control of the peripheral components is performed by the Artix-7 FPGA. Bias voltage together with clock generation units create the signals necessary to drive the CCD, which has four output video channels. These video signals are digitized using 18-bit, 15 MSPS analog-to-digital converters based on successive approximation registers (SAR), tightly coupled with low-noise differential operational amplifiers. Output samples of the converters are fed into the FPGA to perform digital dual slope integrator (DSI) to compute the pixels. The user interacts with the board through a single Ethernet port, which allows sending and receiving commands as well as data. There are two μBlaze processor instantiated in the FPGA: one is the central unit in charge of the control of the system and peripherals and the other is in charge of the sequencer and smart skipper readout. The users specifies the sequencer using a pseudo-XML language description that includes environments (called recipes) to facilitate the specifications of groups of sequences which are repeatedly executed.

The smart readout technique was implemented by making some firmware modification to the LTA controller (Fig.1). The main modifications are introduced in the sequencer block which is in charge of generating the clocking signal to drive the CCD. For the region of interest (ROI) approach, when the number of Skipper samples per pixel is known beforehand, the sequencer block is a state machine that follow recipes specified by the user. However for the energy of interest (EOI) technique, the sequencer must know the actual pixel value to make the decision whether or not the pixel should be read with a higher signal to noise ratio.

REVIEW OF THE SKIPPER CCD: PIXEL VALUE COMPUTATION

The Skipper-CCD is a special type of charge couple device that has an extra charge storage gate that allows multiple non destructive measurements of the same pixel. The sensor has been successfully used to overcome the $2e^-$ to $3e^-$ RMS (Root Mean Square) noise limit of standard CCDs [3]. With the development of the associated readout electronics, a Skipper camera can approach noise levels in the order of 0.04 e^- RMS [1].

The pixel portion of the video signal of the CCD has two main time-intervals: the reference or pedestal level and the signal level. In the pedestal the sense node is reset to a reference voltage while in the signal level the charge is dumped into the sense node. The value of each pixel is usually computed using the dual slope integration (DSI) method [2], sometimes referred as Correlated Double Sampling or CDS:

$$P_1 = \int_{T_i^+}^{2T_i^-} v(t)dt - \int_{0^+}^{T_i^-} v(t)dt, \tag{1}$$

where $v(t)$ is the video signal, T_i is the integration time, the interval $(0, T_i)$ is the pedestal level and the interval $(T_i, 2T_i)$ the signal level, the $\pm$ superscripts are used to denote that the time instants 0, T_i and $2T_i$ are excluded from the integrals. In the digital implementation of the DSI, as in the LTA controller, integrals are replaced by sampling averaging.

The Skipper-CCD has floating gate sensing node that allows multiple non destructive measurements of the same pixel charge which are averaged to reduce the noise to sub-electron levels. In this case, the final pixel value is

$$P_N = \frac{1}{N} \sum_{j=0}^{N-1} P_{1,j} \tag{2}$$

where, for each value of j, $P_{1,j}$ represent a new measurement of the same pixel, each measurement with a standard deviation of the noise of σ_{P_1}. This averaging reduces the standard deviation of the readout noise to [1, 3]

$$\sigma_{P_N} = \sigma_{P_1}/\sqrt{N} \tag{3}$$

due to the independence of the measurements. In [1] it was experimentally verified that the relation in (3) holds for values of N up to 5000.

SIMPLIFIED MODEL FOR THE BASELINE IN THE SKIPPER CCD

In this section we present a simplified model of the baseline, which produces undesirable fluctuations in the pixels value. Baseline exist in every CCD but its effect is more notorious and difficult to compensate when pixels are readout with different values of skipper samples N. The model describes the variation in the final pixel value (2) caused by the coupling of the CCD clocks into the video signal and the AC coupling capacitor in the readout electronics.

Figure 2 shows three (simplified) types of sequences or input stimulus that are applied, at different times and with no overlapping between them, to read out the Skipper-CCD. Although the CCD is driven by pulsed signals, for the present analysis impulsive signals are used to derive simpler results which still capture the baseline behaviour.
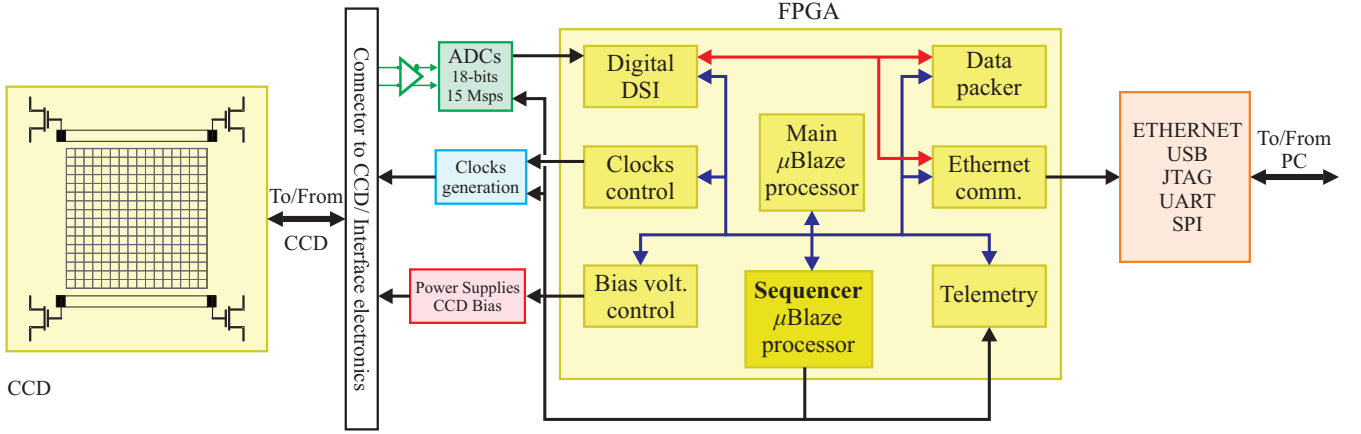
FIG. 1: General diagram of the readout electronics used to implement the smart readout. The main block is the FPGA which among other firmware blocks, has a μBlaze processor dedicated to implement the sequencer.
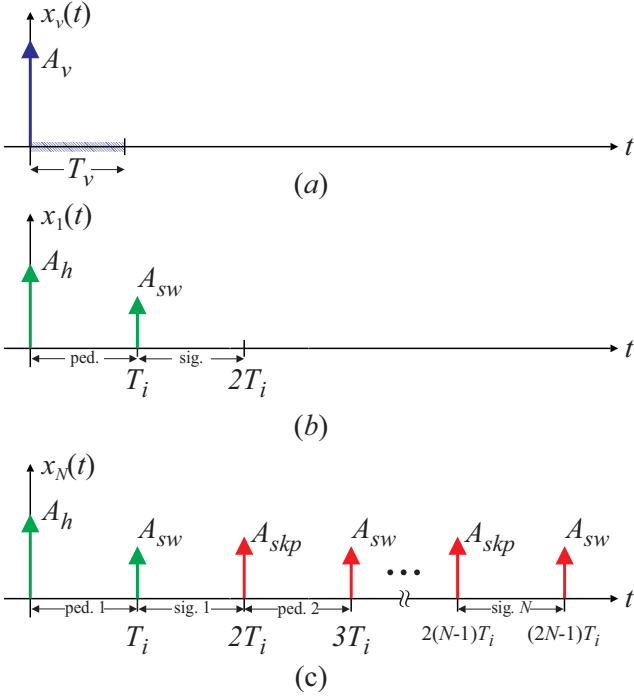

FIG. 2: The three types of input clock sequences, modeled as Dirac-impulses, used to control the CCD. (a) Vertical clocks; (b) Single readout of a pixel and (c) Multiple (N) Skipper readouts of the same pixel.

Since the pulses applied to the CCD have a width much smaller than the time constant τ of the AC coupling circuit, the use of Dirac Delta impulses as stimulus signal for first order analysis is justified. In other words, a pulse of width t_0 and amplitude B is replaced by an impulse of area $A = Bt_0$. The signals in Fig. 2 used for the model do not represent all the clocks applied to the CCD but the main clocks which are useful for the analysis.

Figure 2(a) shows the signal $x_v(t) = A_v\delta(t)$ associated to the vertical clocks of the CCD used to move rows to the

serial register, a response-time T_v, associated to the vertical clocks, during which no pixels are readout is indicated. Figure 2(b) show the main clocks $x_1(t) = A_h\delta(t) + A_{sw}\delta(t - T_i)$ used to readout a pixel a single time. The area A_h is associated to the horizontal clocks, applied before the pedestal interval, and the area A_{sw} to the summing well clock, used to transfer the charge after the pedestal interval to the sense node. The areas used for the impulses stimulus don't directly model the the area of the pulsed signals used to drive the CCD, but how they couple into the video signal. The time T_i is the integration time associated to the pedestal (ped.) and signal levels (sig.), which are integrated by the Dual Slope Integration (DSI) method to calculate pixels values.

In the skipper mode, when the same pixel is read N times, the sequence is as shown in Fig.2(c):

$$x_N(t) = x_1(t) + \sum_{n=2}^{N} A_{skp}\delta(t - 2(n-1)T_i) + A_{sw}\delta(t - (2n-1)T_i).$$

$$(4)$$

In this case from the second readout of the same pixel to the last N readout, the sequence includes the impulse A_{skp} and A_{sw} which models the clocks used in the Skipper output stage to put the charge back and forth into the sense node before the next readout of the same charge packet.

The readout of the row k of the CCD, which can include pixels that are read only once and pixels that are read N times, results in a clock sequence of the form

$$v_k(t) = x_v(t - t_k) + \sum_l x_1(t - (k_l T_i + T_v + t_k))$$

$$+ \sum_m x_N(t - (k_m T_i + T_v + t_k)) \qquad (5)$$

where t_k is the time at which the vertical clocks are applied and k_l and k_m are integers which depends on which pixel of the row a read with either a single sample $N = 1$ or $N > 1$
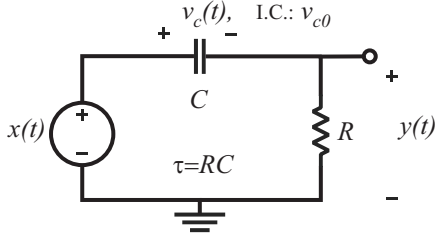
FIG. 3: High pass circuit used for DC decoupling of the video signal.

respectively. The complete input clocking to read the full CCD is the sum of all the clocks used for each line. Each line includes the vertical clocks stimulus (first term in eq. (5)) and the successive readout of each pixel which can be read a single time (first summation in eq. (5)) or N-times (second summation in eq. (5)).

The video decoupling circuit

Non overlapping combination of the sequences $x_v(t)$, $x_1(t)$ and $x_N(t)$ are applied to the CCD and the video signal is readout as a result. Although there are several filters involved in the path of the video signal, for the baseline analysis there is a dynamical system (passive, RC high pass filter) used to decouple the DC voltage from the AC voltage of the video signal, that dominates the performance. The circuit is shown in Fig. 3 which has an associated time constant τ. This filter dominates because it has the longest time constant (much longer than the pixel time $2T_i$) and the baseline drift is dominated by this response. Other filters (low-pass filters with cuts of frequencies in the order of hundreds of kHz) in the analysis will only contribute at shorter time scales (much shorter than $2T_i$) adding complexity to the analysis without significant contribution to the final results.

To model the effect of baseline in the pixel value we analyse the output of the circuit in Fig. 3 when the input $x(t)$ is given by a combinations of stimulus as the one described. The impulse response of the system is

$$h(t) = \delta(t) - \frac{1}{\tau}e^{-t/\tau}\mathcal{H}(t) \tag{6}$$

where $\mathcal{H}(t)$ is the Heaviside or step function. The output of the system for an input $x(t)$, with an initial voltage condition $v_{c0} = v_c(0)$ in the capacitor is

$$y(t) = (x * h)(t) - v_{c0}e^{-t/\tau}\mathcal{H}(t) \tag{7}$$

where $*$ is the convolution operator.

For the smart readout of the Skipper CCD vertical clock sequences $x_v(t)$ appear at the beginning of each row, but single-time pixel readout $x_1(t)$ and multiple-times skipper readout $x_N(t)$ can change arbitrary from pixel to pixel. Since in principle the readout sequence is not known, we can

compute the output for a single sequence using ec. (7) and considering that previous sequences left on the capacitor an initial condition v_{c0}.

For example, the output produced by $x_1(t)$ is

$$y_1(t) = A_h\delta(t) + A_{sw}\delta(t - T_i) - \frac{A_h}{\tau}e^{-t/\tau}\mathcal{H}(t)$$
$$- \frac{A_{sw}}{\tau}e^{-(t-T_i)/\tau}\mathcal{H}(t - T_i) - e^{-t/\tau}v_{c0}\mathcal{H}(t), \tag{8}$$

where the input appears at the output plus three exponential terms: one caused by the horizontal clocking, another by the summing well clocking (sw) and the final one due to the initial condition, caused by previous pixels clocks sequencing.

The pixel value (no charge in the pixel), is computed using DSI in the signal and pedestal intervals as

$$P_1 = \int_{T_i^+}^{2T_i^-} y_1(t)dt - \int_{0^+}^{T_i^-} y_1(t)dt$$

$$P_1 = v_{c0}\tau + A_h - A_{sw} + e^{-2T_i/\tau}(v_{c0}\tau + A_h)$$
$$+ e^{-T_i/\tau}(-2(v_{c0}\tau + A_h) + A_{sw}), \tag{9}$$

this non-zero value is the baseline of the pixel. Among other parameters, baseline depends on the previous pixels through the initial condition in the capacitor v_{c0}.

Sequence of many pixels read only one time each

It is interesting to see how baseline evolves under certain specific sequences of readout. For example, when many consecutive empty pixels are read just one time ($N = 1$): $P_1[n]$ with $n = 1, 2, 3, \cdots$ in the same row, i.e., many $x_1(t)$ sequences are applied consecutively. The values of $P_1[n]$ can be obtained by using the result in eq.(9). Knowing that at the end of each pixel, at $t = 2T_i$, the capacitor voltage is minus the output voltage of the RC circuit and iterating over the initial condition: $v_{c0}[n + 1] = -y_1(2T_i)|_{v_{c0}=v_{c0}[n]}$. Solving this recursive difference equation on the initial condition and assuming $v_{c0}[0] = 0$ results in

$$P_1[n] = \left[A_h\left(1 - e^{-2(1+n)\frac{T_i}{\tau}}\right) - A_{sw}\left(1 - e^{-(1+2n)\frac{T_i}{\tau}}\right)\right]$$
$$\times \tanh\left(\frac{T_i}{2\tau}\right), \tag{10}$$

which is an exponential function on the pixel number n with time constant in units of pixels of $\tau_{pix} = \tau/(2T_i)$. Figure 4 shows the evolution of the baseline for this sequence of pixels revealing the exponential nature. When n is grater than 4 or 5 times τ_{pix} the baseline could be considered to reach an steady state value.
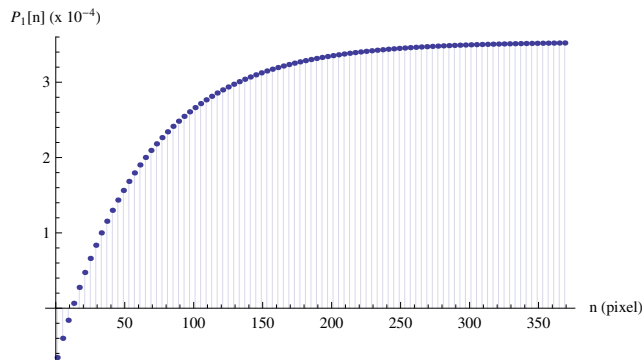
FIG. 4: Baseline example produced by a sequence of pixels all read with $N = 1$ for: $A_h = 0.1$, $A_{sw} = 0.01$, $T_i = 50\mu$s and $\tau = 0.0064$s

Sequence of many pixels read N time each

The result and procedure of the previous section can be used to compute the pixel produced after a sequence as $x_N(t)$ in Fig. 2(c) that correspond to a single pixel measured many times ($N > 1$). The input $x_N(t)$ is the concatenation of $x_1(t)$ plus additional $N-1$ pairs of impulses with areas A_{skp} and A_{swp} (the only change in these pairs, compared to $x_1(t)$ is A_{skp} instead of A_h). Once each of the N measurements of the pixel are computed, they can be averaged to obtain the pixel value P_N.

It is interesting to see how baseline evolves when many consecutive pixels are read with the same value of $N \gg 1$: $P_N[n]$ with $n = 1, 2, 3, \cdots$ in the same row, i.e., many $x_N(t)$ sequences are applied back to back. The results are shown in Fig. 5 for many consecutive pixels read with $N = 100$ and $N = 500$ for: $A_h = 0.1$, $A_{sw} = 0.01$, $T_i = 50\mu$s and $\tau = 0.0064$s. Due to the time compaction produced by the averaging of many measurements of the same pixel, the baseline settles in a steady state value very quickly in terms of the number of pixels. For $N = 500$ the first pixel $P_{500}[1]$ "absorbs" all the transient response and successive pixels of the same kind $P_{500}[2]$, $P_{500}[3]$, $\cdots$ will have an steady state value, this can be seen in Fig. 5b where $P_{500}[1]$ has a different value and then steady state is reached. For $N = 100$ it takes around 3 consecutive pixels $P_{100}[1]$, $P_{100}[2]$ and $P_{100}[3]$ each one read with $N = 100$ to reach an steady baseline value as shown in Fig. 5a.

A CALIBRATION TECHNIQUE FOR BASELINE

This model is useful for understanding how baseline affects the final pixel value, when different and arbitrary changing samples per pixel N are used to readout the Skipper CCD.

The calibration method is based on measuring and making a system identification on how the Skipper-CCD camera responds to the three types of stimulus described on previ-
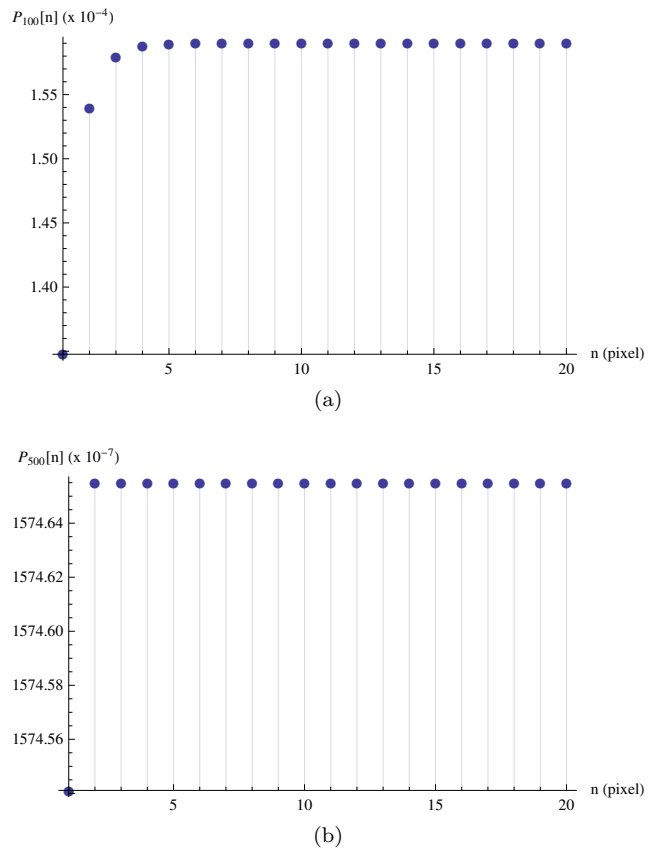

(a)

(b)

FIG. 5: Baseline example produced by a sequence of pixels $P_N[n]$ all read with: a) $N = 100$ and b)$N = 500$ for: $A_h = 0.1$, $A_{sw} = 0.01$, $T_i = 50\mu$s and $\tau = 0.0064$s.

ous section. A superposition of the effects is then used to calibrate the image with any arbitrary N pattern for each pixel. The method does not rely on this model being correct, we only assume linearity time invariance and that the system approaches a steady state after sufficient time.

The calibration was developed for two possible values of N: $N = 1$ and $N = 500$. Specific pattern images with regions measured with $N = 1$ and regions measured with $N = 500$ were acquired to identify the system response.

Calibration images

Figure 6(a) shows a pattern used to characterize part of the sensor baseline response, it consists of 50 rows all measured with the same N distribution: up to column 400 (which includes all the active sensor region) the value of $N = 1$ is used. For columns in the over-scan region, empty pixels outside the active area, columns with $N = 500$ are measured intercalated with columns with $N = 1$. Specifically the following columns are measured with $N = 500$: 401, 402, 404, 407, 411, 416, 422, 429, 437, 446, 456, 467, 479, 492, 506, 521, 537, 554, 572, 591, 611, 636, 666, 701, 741, 786, 836, 891, 951, 1016, 1086, 1161, 1241, 1326, 1416,
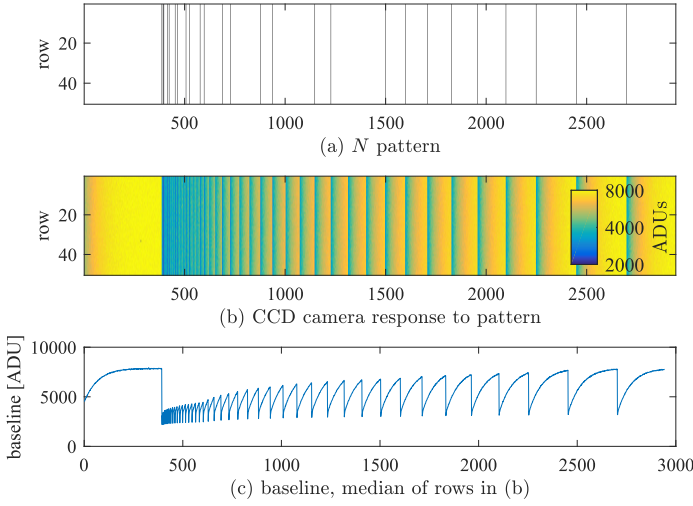
(a) N pattern

(b) CCD camera response to pattern

(c) baseline, median of rows in (b)

FIG. 6: (a) Shows the pattern of N (columns) used for baseline calibration. Black pixels are measured with $N = 500$ and white pixels with $N = 1$ (b) show the sensor response (baseline) to the pattern; (c) shows the baseline computed as the median of all the rows in (b).

(a) N pattern

(b) CCD camera response to pattern
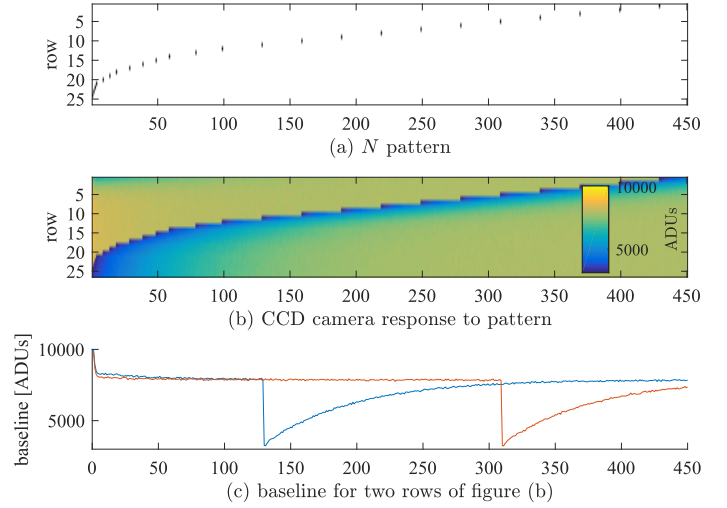

(c) baseline for two rows of figure (b)

FIG. 7: (a) Shows the pattern used for baseline calibration. Black pixels are measured with $N = 500$ and white pixels with $N = 1$. (b) show the sensor response (baseline) to the patterns. (c) shows the baseline for two rows of (b) which have $N = 500$ at column 130 (blue) and 310 (red).

1511, 1611, 1721, 1841, 1971, 2111, 2261, 2461, 2711, 3011, 3361, 3761, 4211. This allows to verify the value of the baseline for pixels measured with $N = 500$ under different initial conditions. All pixels are measured far from the vertical clocks in order to study the initial condition left by different amount of $N = 1$ pixels before the pixel with $N = 500$. The pattern is also useful to study the evolution of many consecutive pixels measured with $N = 1$.

The results are shown in Figures 6(b) that depicts the measured response of the sensor to the pattern, and in Fig. 6(c), that shows the baseline computed as the median of all the rows in (b).

The following observations about this experiment are made:

- From column 1 to column 400, the evolution of the baseline for consecutive pixels measured with $N = 1$ follows the exponential response predicted by the model, simulated in Fig. 4 and described by eq. (10). The "time constant" in pixel of this response is around $\tau_{pix} = 66$ pixels, because of this, after column $4\tau_{pix} = 264$ the baseline reaches steady state.

- In column 401, a pixel with $N = 500$ is measured, as explained in the simulation of Fig.5b, the first pixel read with $N = 500$ "absorbs" the transient produced by switching from sequence $x_1(t)$ to sequence $x_{500}(t)$. The next pixel at column 402 which is also measured with $N = 500$ is in its steady state value.

- After each of the pixels measured with $N = 500$ an exponential response for consecutive pixels measured with $N = 1$ is observed in Fig. 6(c). This response is the same one observed in the active region after the vertical clocks, starting on different initial conditions,

but with the same asymptotic value, which can be reached if there are enough consecutive pixels with $N = 1$.

Figure 7(a) shows a different pattern used to calibrate the baseline. In this case one single-pixel with $N = 500$ is measured in a different column in each row. Specifically, starting from row 26 down to row 1, pixels with $N = 500$ are read in columns: 1, 1, 2, 3, 4, 5, 10, 15, 20, 30, 40, 50, 60, 80, 100, 130, 160, 190, 220, 250, 280, 310, 340, 370, 400, 430. This pixels are at different distances from the vertical clocks $x_v(t)$, and are useful for calibrating the baseline for pixels measured with $N = 500$ with different initial conditions caused by the changing distances to the vertical clocks.

The measured response to the pattern is shown in Fig. 7(b) after taking the median of 24 images with the same pattern. Figure7(c) show the baseline for two rows of the image, specifically for rows with $N = 500$ in columns 130 and 310. Each of the pixels measured with $N = 500$ has a slightly different baseline value caused by its increasing distance to the vertical clocks (column position).

Calibration technique

The objective of the calibration technique is to remove the baseline of images, which were taken in each pixel with an arbitrary number N of samples, using the information acquired with the calibration images. The calibration is stable over time so it can be carried out for an specific setup and updated only if there is a change on the system or on in its operating point. Specifically we developed the
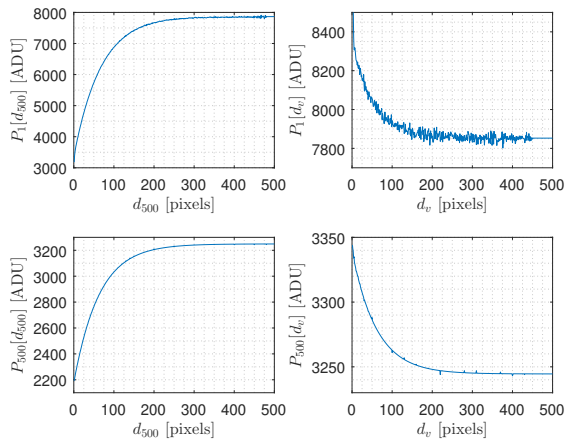
FIG. 8: Measurements of the baseline for pixels with $N = 1$ and $N = 500$ as a function to the distance in pixels to the last pixel measured with $N = 500$: distance d_{500} and as a function of the column number or equivalently distance to vertical clocks d_v.

technique for pixels measured with $N = 1$ or $N = 500$ but the approach could be applied for other values of N.

There is more than one way to correct the baseline based on the model and analysis developed in the previous sections. The approach developed is based on the fact that a single $N = 500$ pixels leaves the baseline in known stationary value. Four lookup tables were generated from the information available in the system response to the patterns of Fig. 6 and Fig. 7 to perform the calibration. Figure 8 shows the results extracted from the response to the pattern images. Two tables are generated for pixels measured with $N = 500$ and two for pixels measured with $N = 1$. Each of the two tables have the baseline for different initial conditions that depend on: 1) how many pixels before the actual pixel was the last pixel with $N = 500$ (distance d_{500}) and 2) the column position of the pixel (or equivalently distance to the vertical d_v). The pattern images allow to measure this two calibration values isolated from each other, i.e., the effect of d_{500} when pixels are far from the verticals clocks, and therefore the vertical effect is in steady state, and vice-versa. Parameterizing the calibration in this two distances allow for easy compensation since the only thing that need to be tracked is d_{500} since d_v is the column position of the pixel.

The result in the top of Fig. 8, for $N = 1$ shows $P_1[d_v]$ and $P_1[d_{500}]$, although the initial condition produced by d_{500} and by d_v are different, after $\approx 4\tau_{pix} = 264$ both curves reach the same steady state value of $P_1^{ss} \approx 7850$ ADU

which is the expected value for many consecutive pixels $P_1[n]$ measured with $N = 1$. A similar situation is seen at the bottom of Fig. 8, for $P_{500}[d_v]$ and $P_{500}[d_{500}]$ but in this case achieving an steady state of $P_{500}^{ss} \approx 3247$ ADU

The experimental results showed that the effects of d_{500} and d_v on the pixel value are independent, justifying the approach of linearity and time invariance assumed before. Therefore the results of Fig.8 can be combined to get the calibration for any possible combination of $N = 1$ and $N = 500$ used for the readout of the CCD. The baseline for each pixel can be estimated as

$$ BL = \begin{cases} P_N[d_{500} + \Delta V] + P_N[d_v] - P_N^{ss} & \text{if } d_{500} \geq d_v \\ P_N[d_{500}] & \text{if } d_{500} < d_v \end{cases} $$

(11)

where N equals 1 or 500 depending on the value used for the current pixel, and $\Delta V = \text{Round}(T_v/(2Ti))$ is the time T_v required for the vertical clocks (see Fig. 2) expressed in number of pixels. When $d_{500} \geq d_v$ the last pixel measured with $N = 500$ was in the previous CCD row, so the vertical clocks $x_v(t)$ appear between it and the actual pixel. For this case the compensation includes both the effect combined: $P_N[d_{500} + \Delta V]$ models the effect of last pixel measured with $N = 500$ on the actual pixel and $P_N[d_v] - P_N^{ss}$ adds the effect of the vertical clock. When $d_{500} < d_v$ there was, in the same row, a previous pixel read with $N = 500$ which absorbs all the vertical clock transient and then the vertical calibration is not necessary ($P_N[d_v] - P_N^{ss} = 0$).

In summary, the value of baseline BL is computed for every pixel by tracking d_{500}, the column of the pixel d_v and using the calibration in Fig. 8 in eq.(11). Finally BL is subtracted from each pixel to correct its value.

————————

[1] Gustavo I. Cancelo, Claudio Chavez, Fernando Chierchie, Juan Estrada, Guillermo Fernandez-Moroni, Eduardo E. Paolini, Miguel Sofo Haro, Angel Soto, Leandro Stefanazzi, Javier Tiffenberg, Ken Treptow, Neal Wilcer, and Ted J. Zmuda. Low threshold acquisition controller for Skipper charge-coupled devices. *Journal of Astronomical Telescopes, Instruments, and Systems*, 7(1):1 – 19, 2021.
[2] James R Janesick. *Scientific charge-coupled devices*, volume 83. SPIE press, 2001.
[3] Javier Tiffenberg, Miguel Sofo-Haro, Alex Drlica-Wagner, Rouven Essig, Yann Guardincerri, Steve Holland, Tomer Volansky, and Tien-Tien Yu. Single-electron and single-photon sensitivity with a silicon Skipper CCD. *Phys. Rev. Lett.*, 119(13):131802, 2017.